

Escape patterns of chaotic magnetic field lines in a tokamak with reversed magnetic shear and an ergodic limiter

T. Kroetz,¹ M. Roberto,¹ E. C. da Silva,² I. L. Caldas,² and R. L. Viana³

¹*Instituto Tecnológico de Aeronáutica, Centro Técnico Aeroespacial, Departamento de Física, 12228-900, São José dos Campos, São Paulo, Brazil*

²*Instituto de Física, Universidade de São Paulo, 05315-970, São Paulo, São Paulo, Brazil*

³*Departamento de Física, Universidade Federal do Paraná, 81531-990, Curitiba, Paraná, Brazil*

(Received 12 June 2008; accepted 29 August 2008; published online 25 September 2008)

The existence of a reversed magnetic shear in tokamaks improves the plasma confinement through the formation of internal transport barriers that reduce radial particle and heat transport. However, the transport poloidal profile is much influenced by the presence of chaotic magnetic field lines at the plasma edge caused by external perturbations. Contrary to many expectations, it has been observed that such a chaotic region does not uniformize heat and particle deposition on the inner tokamak wall. The deposition is characterized instead by structured patterns called magnetic footprints, here investigated for a nonmonotonic analytical plasma equilibrium perturbed by an ergodic limiter. The magnetic footprints appear due to the underlying mathematical skeleton of chaotic magnetic field lines determined by the manifold tangles. For the investigated edge safety factor ranges, these effects on the wall are associated with the field line stickiness and escape channels due to internal island chains near the flux surfaces. Comparisons between magnetic footprints and escape basins from different equilibrium and ergodic limiter characteristic parameters show that highly concentrated magnetic footprints can be avoided by properly choosing these parameters. © 2008 American Institute of Physics. [DOI: 10.1063/1.2988335]

I. INTRODUCTION

In the last decade several experiments have confirmed that modifications of radial electrical current profiles can improve the plasma confinement in tokamaks. In particular, it has been shown that the presence of reversed magnetic shear can reduce fluctuation levels and the fluctuation-driven transport.^{1–5} Reversals of magnetic shear over a wide region of the plasma column occur in plasmas with nonmonotonic safety factor profiles.⁶ Such profiles can result from noninductive current drive methods like neutral beam injection. The combination of Ohmic heating and current drive generate configurations with enhanced reversed shear and highly peaked density and pressure profiles. These discharges present reduction of the plasma transport, through the formation of a transport barrier, i.e., a region where both the electron and ion diffusivities are greatly reduced around the shearless radius.^{1–3,7,8} Moreover, these kinds of discharges have been observed in transitions from low (L) to high (H) regimes, for which limited regions of the plasma, specially at the edge, may exhibit reversed shear through proper modification of the radial profiles.⁹

Other modifications can also be achieved by applying different kinds of perturbations at the plasma edge. In particular, external electrical currents can be used to create additional resonant magnetic perturbations inside the plasma. Such resonances create a zone of chaotic magnetic field lines at the plasma edge that controls stability or transport of heat and particles therein. Such external resonant perturbations can be produced by ergodic limiters,^{10–13} that have been shown to improve plasma confinement,¹⁴ as well as to control magnetic activity¹⁵ and plasma disruptions.^{16–19} Further-

more, a recent experiment has shown that ergodic divertors can also be successfully applied to mitigate edge localized modes while maintaining the plasma confinement.²⁰

Originally, the ergodic limiter was proposed as a procedure to obtain a uniform distribution of the exhausted power on the wall.^{10,21–23} The field line ergodization resulting from the resonant perturbation created by such a divertor would lead to a broadening of the scrape-off layer and a widening of the contact zone between plasma and the wall.²⁴ Devices based on this concept have been tested on several machines.^{19,21–23,25–27} However, further experiments have revealed that the heat and particle deposition patterns are not actually uniform as previously assumed, but are rather strongly structured, presenting a self-similarity that suggests an underlying fractal structure.^{28–35}

These structured patterns of the heat and particle deposition turn out to be undesirable from the point of view of controlling plasma-wall interactions, and have been investigated in a series of experiments with the dynamic ergodic divertor.^{32–35} Although the patterns are not uniform, they proved to be manageable through changing the plasma equilibrium or varying the resonant perturbations, such that one can control heat and particle deposition on the tokamak vessel.³⁶

The usefulness of ergodic divertors in the improvement of the plasma confinement, particularly with reversed shear magnetic fields, makes the understanding and control of the deposition pattern a key issue in advanced tokamak scenarios. The spatial structures observed in the heat flux deposition patterns on the tokamak wall have been interpreted as a consequence of the topology of the perturbed magnetic

field and the structure of the field lines.³⁷ This results from the fact that charged particles predominantly follow the magnetic lines, and thus a description of how field lines escape would give an approximate description of the experimentally observed heat deposition patterns on the tokamak wall. The latter have been identified through the so-called *magnetic footprints*.

Magnetic footprints have been obtained by using numerically^{29,38–46} and analytically^{47–50} obtained maps of the perturbed magnetic fields. The observed fractal structure of magnetic footprints follows from the mathematical structure underlying the area-filling chaotic region of magnetic field lines—a chaotic manifold tangle, comprising the homoclinic and heteroclinic intersections of invariant manifolds of unstable periodic orbits embedded in the chaotic region.^{29,38,39} Another consequence of this manifold tangle is an involved structure of escape basins, which indicate the loci of points such that a field line passing through that point will escape through a given region at the tokamak wall.⁵¹

In this paper we investigate the magnetic footprints and related escape basins for a tokamak with reversed magnetic shear, obtained through using a nonmonotonic plasma current profile. The chaotic magnetic field in the reversed shear region is generated by an ergodic limiter, which is an external current configuration whose magnetic field resonates with the equilibrium field yielding a magnetic island structure and invariant flux surfaces.^{51,52} Chaotic field lines (in the Lagrangian sense, since our configuration is strictly magnetostatic) result from interactions among magnetic islands, with progressive destruction of perturbed flux surfaces as the perturbation strength increases, according to a peculiar scenario described in Refs. 52–56 and which is different from that observed in twist magnetic configurations, where the Kolmogorov–Arnold–Moser (KAM) theory is valid.^{57–59} This difference occurs around the magnetic shearless surface. However, at the plasma region far from the shearless surface, the KAM theory can be applied.

This paper is organized as follows: In Sec. II we describe the model fields for a nonmonotonic plasma equilibrium and the perturbation caused by an ergodic limiter. Section III deals with the structure of magnetic field lines resulting from such model fields, using a symplectic map obtained from a Hamiltonian description. The magnetic footprints and escape basins for the configuration we investigate are described in Sec. IV. The last section is devoted to our conclusions.

II. MODEL FIELDS

We use a nonorthogonal coordinate system to describe magnetic field lines in a tokamak, $(r_t, \theta_t, \varphi_t)$, related to the usual local coordinates (r, θ, φ) by the following relations:⁶⁰

$$r_t = r \left[1 - \frac{r}{R'_0} \cos \theta + \left(\frac{r}{2R'_0} \right)^2 \right]^{1/2}, \quad (1)$$

$$\sin \theta_t = \sin \theta \left[1 - \frac{r}{R'_0} \cos \theta + \left(\frac{r}{2R'_0} \right)^2 \right]^{-1/2}, \quad (2)$$

where R'_0 is the magnetic axis radius. In the large aspect ratio limit ($r_t \ll R'_0$), r_t and θ_t become r and θ , respectively. The

relation of the magnetic axis radius with the major radius R is

$$R^2 = R_0'^2 \left[1 - 2 \frac{r_t}{R'_0} \cos \theta_t - \left(\frac{r_t}{R'_0} \right)^2 \sin^2 \theta_t \right], \quad (3)$$

which leads to physically meaningful results provided $r_t/R'_0 < 1/2$, a condition always fulfilled in the numerical simulations to be described in this paper.

Assuming axisymmetry, the contravariant components of the equilibrium magnetic field \mathbf{B}_0 can be obtained from a poloidal flux $\Psi_p(r_t, \theta_t)$ and the poloidal current function $I(r_t, \theta_t)$ as

$$B_0^1(r_t, \theta_t) = - \frac{1}{R'_0 r_t} \frac{\partial \Psi_p}{\partial \theta_t}, \quad (4)$$

$$B_0^2(r_t, \theta_t) = \frac{1}{R'_0 r_t} \frac{\partial \Psi_p}{\partial r_t}, \quad (5)$$

$$B_0^3(r_t, \theta_t) = - \frac{\mu_0 I}{R^2}. \quad (6)$$

The poloidal flux results from solving the equilibrium equation in these coordinates.⁶⁰ We obtained an approximate solution by considering the first-order expansion $\Psi_p(r_t, \theta_t) = \Psi_{p0}(r_t) + \delta \Psi_p(r_t, \theta_t)$, where $\Psi_{p0}(r_t)$ is a solution corresponding to the cylindrical case

$$\frac{1}{r_t} \frac{d}{dr_t} \left(r_t \frac{d \Psi_{p0}}{dr_t} \right) = \mu_0 J(\Psi_{p0}), \quad (7)$$

and $|\delta \Psi_p(r_t, \theta_t)| \ll |\Psi_{p0}(r_t)|$ contains the toroidal corrections, and $J[\Psi_{p0}(r_t)]$ is the toroidal current density profile. Since we are focusing on equilibrium fields possessing reversed shear, we assume a nonmonotonic current profile,⁶²

$$J(r_t) = \frac{I_p R'_0 (\gamma + 2)(\gamma + 1)}{\pi a^2 \beta + \gamma + 2} \left(1 + \beta \frac{r_t^2}{a^2} \right) \left(1 - \frac{r_t^2}{a^2} \right)^\gamma, \quad (8)$$

where I_p is the total plasma current, a is the plasma radius, and β and γ are positive parameters.

The intersections of the flux surfaces $\Psi_p(r_t) = \text{constant}$ with a toroidal plane exhibit the Shafranov shift toward the exterior equatorial region (Fig. 1). Moreover, the safety factor profile is given by

$$q(r_t) = \frac{1}{2\pi} \int_0^{2\pi} \frac{B_0^3(r_t, \theta_t)}{B_0^2(r_t)} d\theta_t = q_c(r_t) \left(1 - \frac{4r_t^2}{R_0'^2} \right)^{-1/2}, \quad (9)$$

where $q_c(r_t)$, for the nonmonotonic profile (8), is given by⁶²

$$q_c(r_t) = q_c(a) \frac{r_t^2}{a^2} \times \left[1 - \left(1 + \beta' \frac{r_t^2}{a^2} \right) \left(1 - \frac{r_t^2}{a^2} \right)^{\gamma+1} \Theta \left(1 - \frac{r_t}{a} \right) \right]^{-1} \quad (10)$$

with $q_c(a) \equiv I_p a^2 / I_e R_0'^2$, $\beta' \equiv \beta(\gamma + 1) / (\beta + \gamma + 2)$, and $\Theta(\cdot)$ is the unit step function, yielding a nonmonotonic safety factor profile (Fig. 2). In the numerical simulations, we normalize

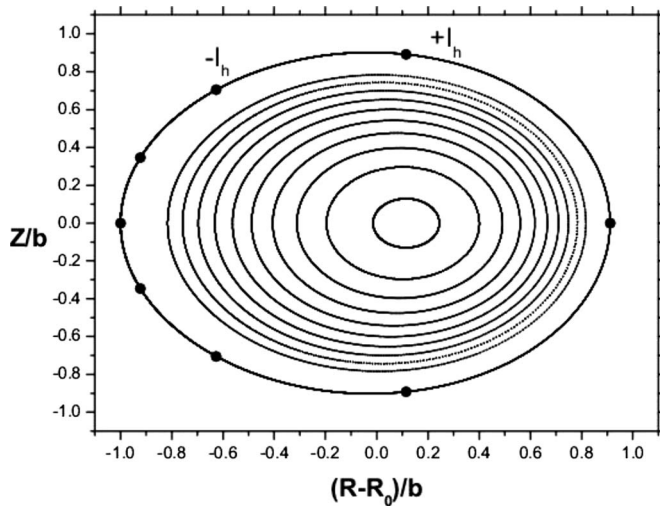


FIG. 1. Equilibrium flux surfaces for the plasma equilibrium with reversed shear given by a nonmonotonic current profile.

the minor tokamak radius b and the plasma radius a to the major (magnetic axis) radius R'_0 , such that $a/R'_0=0.28$ and $b/R'_0=0.35$. We also choose $q(a)=5.0$ and $q(0)=4.75$, corresponding to the safety factors at the plasma edge and magnetic axis, respectively, when $\beta=3.0$ and $\gamma=0.8$. With this set of parameters we see, from Fig. 2, that the shearless radius is near the middle of the plasma column ($r/a \approx 0.6$). At both sides of the shearless radius there are flux surfaces with the same safety factor, as $q=4.0$ for example, leading to the formation of dimerized island chains, when a magnetic perturbation is applied. These islands are centered at the position of the corresponding resonant flux surfaces.

The magnetic perturbation we considered in this paper is produced by an ergodic limiter consisting of N_r current rings of length ℓ located symmetrically along the toroidal direction of the tokamak (Fig. 3). Each current ring can be considered as slice of a resonant helical winding with mode numbers (m_0, n_0) and a winding law given by $u_i = m_0(\theta_i + \lambda \sin \theta_i) - n_0 \varphi_i = \text{constant}$, where λ is a tunable parameter. These cur-

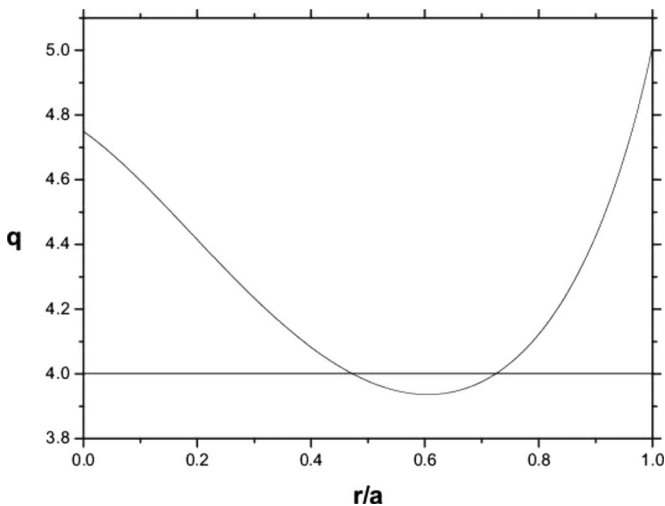


FIG. 2. Nonmonotonic safety factor profile for a reversed shear equilibrium with $\beta=3$ and $\gamma=0.8$.

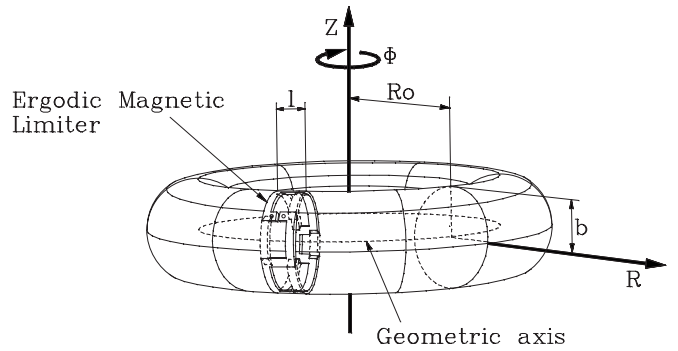


FIG. 3. Scheme of an ergodic magnetic limiter.

rent rings are located at the vessel radius $r_i = b_i$ and carry a current I_h in opposite senses for adjacent conductors. The role of these windings is to induce a dominant (m_0, n_0) resonant perturbation in the tokamak, and to achieve this effect we must choose a helical winding with the same pitch as the field lines in the rational surface we want to perturb.

The perturbing magnetic field generated by the ergodic limiter is assumed to be a vacuum field solution $\mathbf{B}_L = \nabla \times \mathbf{A}_L$ of the Laplace equation with proper boundary conditions at the tokamak wall. The vector potential can be written as a sum of a large number of resonant terms whose amplitudes, being proportional to Bessel functions of order k , decay with increasing k .⁶¹ Thus, inside the plasma, it is a good approximation to consider, in lowest order, the only nonvanishing component of the corresponding vector potential given by⁶²

$$A_{L3}(r_i, \theta_i, \varphi_i) \approx -\frac{\mu_0 I_h R'_0}{\pi} \left(\frac{r_i}{b_i}\right)^{m_0} \cos(m_0 \theta_i - n_0 \varphi_i). \quad (11)$$

The magnetic field line equations corresponding to the superposition of the equilibrium and limiter fields, $\mathbf{B} = \mathbf{B}_0 + \mathbf{B}_L$, are

$$\frac{dr_i}{d\varphi_i} = -\frac{1}{r_i B_T} \left(1 - 2 \frac{r_i}{R'_0} \cos \theta_i\right) \frac{\partial}{\partial \theta_i} A_{L3}(r_i, \theta_i, \varphi_i), \quad (12)$$

$$\frac{d\theta_i}{d\varphi_i} = \frac{1}{r_i B_T} \left(1 - 2 \frac{r_i}{R'_0} \cos \theta_i\right) \frac{\partial}{\partial r_i} [\Psi_{p0}(r_i) + A_{L3}(r_i, \theta_i, \varphi_i)], \quad (13)$$

where B_T is the toroidal magnetic field at the magnetic axis.

III. FIELD LINE MAPPING

The field line equations in an axisymmetric configuration are known to exhibit a Hamiltonian (canonical) structure, the symplectic property being a consequence of $\nabla \cdot \mathbf{B} = 0$.^{57,58} The differential equations (12) and (13) can be integrated numerically, but this method can introduce truncation errors that may spoil their symplectic nature. An alternative procedure consists of obtaining a field line map which preserves by construction the symplectic property of the field line equations.⁴⁰

The equilibrium magnetic field represents an integrable Hamiltonian system in the sense that magnetic field lines lie

on surfaces with $H_0 = \text{constant}$. In this case, we can define action-angle variables (\mathcal{J}, ϑ) , and the azimuthal angle $\varphi_i = t$ is a timelike variable parameterizing field lines. The explicit form of the relation between the canonical variables (\mathcal{J}, ϑ) and the coordinates (r_i, θ_i) can be found in Ref. 62.

The magnetic field produced by the ergodic limiter can be regarded as a small perturbation of the integrable Hamiltonian. Since the ergodic limiter current I_h is much smaller than the plasma current I_p , the condition $|A_{L3}/\Psi_{p0}| \ll 1$ is always fulfilled. In this case the perturbed Hamiltonian can be written as

$$\begin{aligned} H(\mathcal{J}, \vartheta, t) &= H_0(\mathcal{J}) + H_1(\mathcal{J}, \vartheta, t), \\ &= \frac{1}{B_T R_0'^2} \Psi_{p0}(\mathcal{J}) + \frac{1}{B_T R_0'^2} A_{L3}(\mathcal{J}, \vartheta, t), \end{aligned} \quad (14)$$

($|H_1/H_0| \ll 1$) such that the magnetic field line equations (12) and (13) can be written in the canonical form

$$\frac{d\mathcal{J}}{dt} = -\frac{\partial H}{\partial \vartheta}, \quad (15)$$

$$\frac{d\vartheta}{dt} = \frac{\partial H}{\partial \mathcal{J}}. \quad (16)$$

For an arbitrary dependence on t of the ergodic limiter perturbation one is forced to resort to numerical integration methods preserving the symplectic area.^{40,63} On the other hand, if the dependence on t can be modelled as a sequence of delta functions the magnetic field lines can be integrated so as to yield an analytical field line map. This is actually possible since the ergodic limiter perturbation is due to N_r rings of a length ℓ which is small compared to the toroidal circumference $2\pi R_0'$, and symmetrically distributed along the toroidal direction. Thus, under each coil the field line position changes due to the action of the kick perturbation described by the delta function. Between coils, where the perturbing field is small, the field lines are mapped under the influence of a rotational transform with shear (tokamak measurements justify this approximation^{13,19}). Corrections due to integration of field lines under the coils give rise to small connections on the Poincaré maps.^{19,13}

The resulting Hamiltonian is

$$H_L(\mathcal{J}, \vartheta, t) = H_0(\mathcal{J}) + \frac{\ell}{R_0'} H_1(\mathcal{J}, \vartheta, t) \sum_{k=-\infty}^{+\infty} \delta\left(t - k \frac{2\pi}{N_r}\right), \quad (17)$$

where the limiter field is approximated by a periodic train of delta kicks applied at each ring position.^{39,51,62,64} An approximated solution of the canonical equations related to the Hamiltonian (14) gives a local approximation of the field line mapping,⁶² which allows a detailed analysis of field line transport and escape.⁶⁵

Due to the delta functions appearing in the Hamiltonian (17), the field lines receive a kick whenever they cross a toroidal section $\varphi = \text{constant}$. Just after the n th kick, the action-angle variables describing the field line position take on the values $(\mathcal{J}_n, \vartheta_n)$, respectively. Between two successive

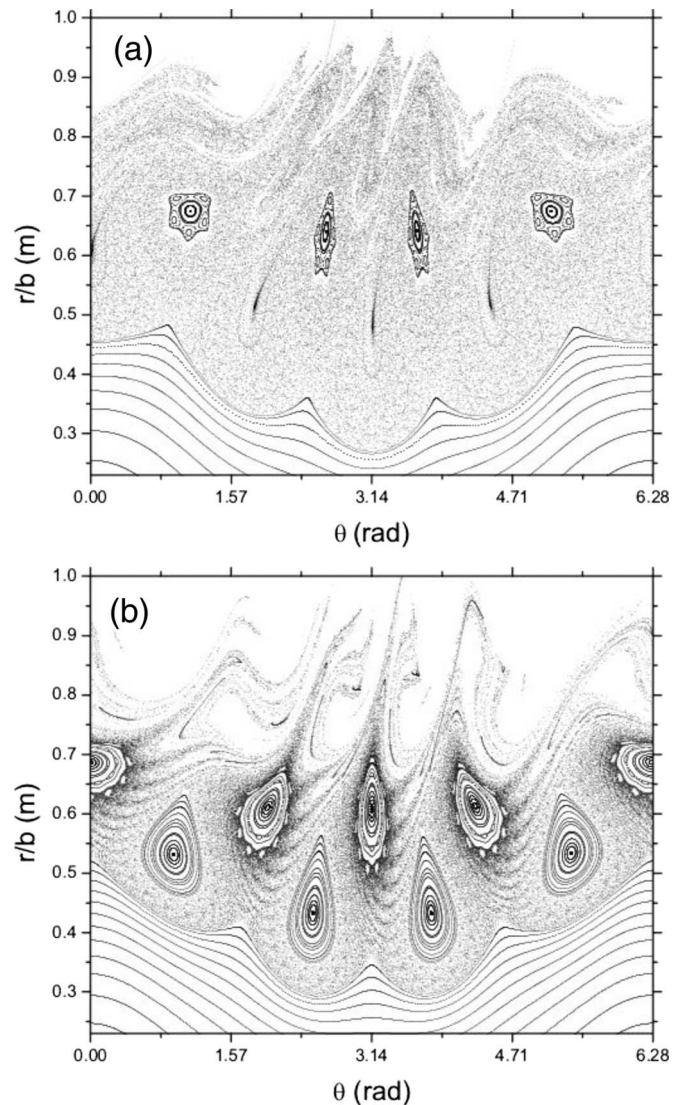


FIG. 4. Poincaré section of a tokamak perturbed by an ergodic limiter for a nonmonotonic safety factor profile with $\gamma=0.80$ and $\beta=3.00$, $N_r=4$, $I_h/I_p=0.11$, and (a) $(m_0, n_0)=(4, 1)$ and $\lambda=0.45319$; (b) $\lambda=0.5895$, $(m_0, n_0)=(5, 1)$.

kicks the field equations can be integrated analytically and, after having received the next kick, the field lines lie on another magnetic surface. The new values of the action-angle variables, $(\mathcal{J}_{n+1}, \vartheta_{n+1})$, are used as a new set of initial conditions, in order to obtain the next action-angle variables. In the following we transform the original action-angle variables (\mathcal{J}, ϑ) to the polar-toroidal (r, θ) coordinates and then to the local coordinates (r, θ) using Eqs. (1) and (2). Thus, after the exact coordinate transformation, we present our results in the original (r, θ) space.

In Fig. 4(a) we show Poincaré sections of the field lines using the canonical map obtained from the Hamiltonian function (17), in the form $(\mathcal{J}_{n+1}, \vartheta_{n+1}) = \mathbf{F}(\mathcal{J}_n, \vartheta_n)$, the explicit form of \mathbf{F} being found in Ref. 62. We make the limiter field to resonate with the flux surface with safety factor $q=4$ by choosing the perturbation parameters as $\lambda=0.45$ and the mode numbers $(m_0=4, n_0=1)$. As a result, there are chains of four dimerized magnetic islands, since, for the considered nonmonotonic equilibrium, there are two distinct ra-

dial locations for the same value of the safety profile. Due to the large limiter current used in this phase portrait ($I_h/I_p = 0.11$) both islands have been considerably destroyed, one of them having been almost completely engulfed by the chaotic region. Hence, this limiter current is large enough so as to generate a chaotic region closer to the wall. Figure 4(b) shows the phase space plot for $\lambda=0.59$, where the limiter has mode numbers ($m_0=5, n_0=1$) and the same current as before. In this mapping the perturbation current is large enough to utterly destroy the (5,1) chain and create a wide chaotic region. The secondary 4/1 dimerized island, however, is less destroyed in comparison with the 5/1 one, as can be seen in Fig. 4(b).

In order to understand the nature of chaotic orbits and its consequence on the transport of field lines, we show the graphical representation of invariant manifolds stemming from an unstable saddle point embedded in the chaotic region. The invariant manifolds are sets of points whose forward and backward iterations belong to the same set. For stable (unstable) manifolds, forward (backward) iterates converge to a hyperbolic saddle point, as the number of iterations goes to infinity. A method to obtain a numerical approximation to these invariant manifolds is to consider the first N_0 (say, 80) forward and backward images of a small disk filled with a large number of initial conditions (say, 5000×5000) and centered at the location of a saddle point embedded in the chaotic orbit.⁶⁶

For large enough limiter currents there is a chaotic region in the outer tokamak region, as can be seen in Figs. 4(a) and 4(b). Choosing a saddle in the midst of this chaotic region, the manifolds stemming from this point are depicted in Figs. 5(a) and 5(b) for the same set of parameters used in Figs. 4(a) and 4(b), respectively. In both figures the dark and gray curves stand for the stable and unstable manifolds, respectively, and the field lines follow closely these manifolds. There are forward (backward) iterations of the map producing trajectories arbitrarily close to a branch of the unstable (stable) manifold. The intersections of unstable and stable manifolds are shown in Figs. 6(a) and 6(b) for the same parameters used in Figs. 4(a) and 4(b), respectively. The fractal structure resulting from the convoluted nature of the manifold branches has practical consequences in the deposition patterns at the tokamak wall since guiding center motion is primarily determined by the field line configuration.

From the dynamical systems point of view, the stable and invariant manifolds, intersecting at homoclinic and heteroclinic points, form a nonattracting chaotic set, also called *manifold tangle*.^{57,59} If we were to choose at random an initial condition placed in the chaotic region, the probability of this point to belong to the manifold tangle is exactly zero. Nevertheless, the manifold tangle has a deep influence on the dynamics in the chaotic region. It is actually the dynamical structure underlying the chaotic orbit. For example, if the manifold tangle were uniformly distributed over the chaotic region, the latter would yield a “normal” (or Gaussian) diffusion of field lines. This occurs, for example, for uniformly hyperbolic chaotic systems, such as the Arnold’s cat map or the Sinai’s billiard.⁶⁷ If this situation were to occur in the chaotic layer generated by an ergodic limiter, the correspond-

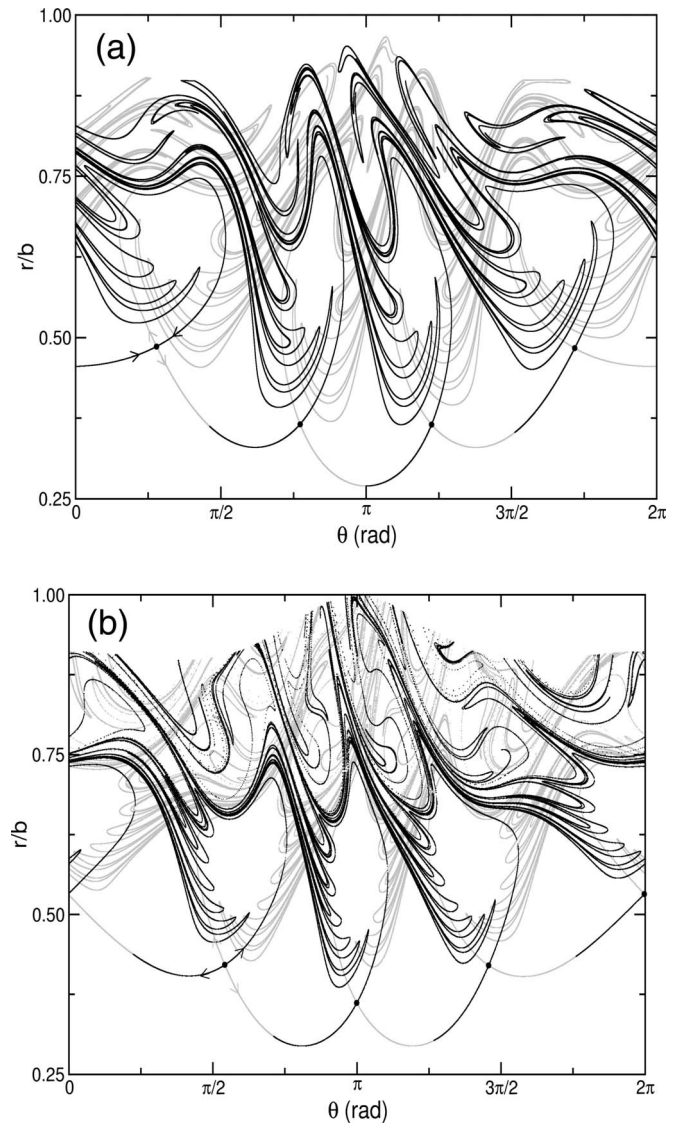


FIG. 5. Invariant stable (dark curves) and unstable (light gray curves) manifolds of a fixed point embedded in the chaotic region corresponding to the Poincaré sections depicted in (a) Fig. 4(a); (b) Fig. 4(b).

ing deposition pattern on the tokamak wall would be accordingly uniform, as it was originally expected.

However, in nonhyperbolic area-preserving systems like the field line map obtained from the Hamiltonian (17), the manifold tangle is nonuniformly distributed, presenting pronounced filaments of manifold branches that form a kind of escape channel, which can be seen in Figs. 5 and 6. These channels, whenever hitting the tokamak wall, are able to drive particles toward the wall, producing the complicated structure of magnetic footprints that is actually observed in experiments. Moreover, the diffusion expected from a nonuniform finite chaotic region at the plasma edge is anomalous, presenting typically a non-Gaussian dependence of the radial quadratic displacement with the timelike variable.^{61,68} However, this is only a local approximation since the calculations are valid for an unbounded space domain.

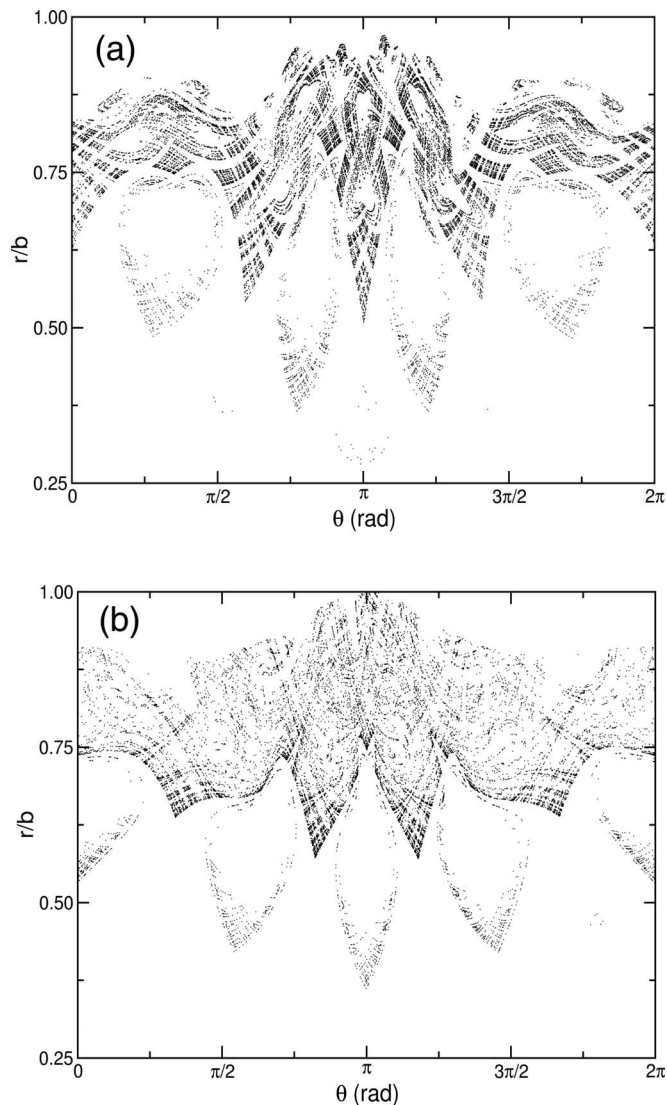


FIG. 6. Intersections among the invariant manifolds corresponding to the Poincaré sections depicted in (a) Fig. 4(a); (b) Fig. 4(b).

IV. ESCAPE OF THE CHAOTIC FIELD LINES

Another observable manifestation of the nonuniformity of the outer chaotic region due to an ergodic limiter is the distribution of the connection lengths of field lines in the plasma edge. The connection length, $N_{cl}(r, \theta)$, is the number of toroidal turns it takes for a field line, originating from a given initial condition located at (r, θ) in the Poincaré section, to reach the tokamak wall. In our case we can set the tokamak wall at the same radius of the ergodic limiter rings, at $r_t = b_t$. The field line is considered lost when it reaches this radial position. The connection length furnishes a rough estimate of the escape time for a particle, passing through the point (r, θ) , to hit the tokamak wall, $\tau \sim 2\pi RN_{cl}/v_T$, where v_T is the thermal velocity. Recent experiments have shown that the radial structure of the electron temperature and density at different times of the discharge reveals a correlation between the connection length and the heat flux.⁶⁹ It has been observed that most of the heat content is brought from the plasma core wall by the field lines with relatively large connection lengths (namely, those with $N_{cl} > 4$).

The connection length depends on the position at the chaotic region in the Poincaré section and, since the chaotic region is nonuniform, as shown in the previous section, we expect a nonuniform distribution of connection lengths in our system. We have numerically computed the distribution of the connection lengths for the situations depicted in Figs. 4(a) and 4(b), by using grids of points on the chaotic region of the corresponding phase portraits, each point serving as a different initial condition. The connection length for each point is the number of toroidal turns necessary for each resulting field line to reach the wall at $r_t = b_t$. In fact, the connection lengths take on values in a wide interval, from $N_{cl} = 1$ to $N_{cl} \approx 10^4$, as illustrated by Figs. 7(a) and 7(b), where $I_h/I_p = 0.11$, and the limiter has mode numbers (4,1) and (5,1), respectively. The connection lengths for each point of this grid, within the interval from 1 to 10 turns, are indicated using a color scale. We have chosen a bounded radial portion of the toroidal section, since we are interested in the escape of the field lines near the tokamak wall (initial conditions with $N_{cl} > 10$ belong altogether in black regions). The regions with short and long connection lengths are also called *laminar* and *ergodic*, respectively.

A common trait of Figs. 7(a) and 7(b) is that both exhibit escape regions with smooth boundaries. Fractal structures can be seen, however, provided larger values of N_{cl} are taken, as in Figs. 7(c) and 7(d), where the interval of connection lengths is increased to an upper limit of $N_{cl} = 200$ toroidal turns. From these examples we can see that not only the connection lengths of the field lines are important, but also their radial penetration depths. For example, there are field lines with small connection lengths starting near the wall or in the vicinity of the island chains. Those field lines produce quite a uniform escape pattern, i.e., without a noticeable concentration on a given region of the wall, and hence should not contribute to the heating deposition patterns observed on the wall. The field lines around the islands with high penetration depths are more evident for the (4,1) mode [Fig. 7(c)] than for the (5,1) one [Fig. 7(d)]. Field lines with connection lengths higher than a given limit (say, $N_{cl} = 4000$), can be considered as effectively trapped. Hence a region with large connection lengths in the toroidal section represents an effective transport barrier.

A further characteristic of the nonuniform escape patterns is their dependence on the safety factor at plasma radius, $q(a)$. We investigated this dependence by making the following numerical experiment: We picked a large number of initial conditions at the tokamak wall with uniformly distributed poloidal angles and computed the connection length of each (i.e., the number of toroidal turns for the line to return to the tokamak wall). The intervals of points with same connection lengths (expressed in a color scale) are depicted in Figs. 8(a) and 8(c) as a function of $q(a)$ for the mode numbers (4,1) and (5,1), respectively, with magnifications shown in Figs. 8(b) and 8(d), respectively. We have varied $q(a)$ so as not to change the limiter current I_h , hence we have instead to vary the plasma current I_p ; from $I_h/I_p = 0.066$ for $q(a) = 3.0$, to $I_h/I_p = 0.110$ for $q(a) = 5.0$.

We can identify in Fig. 8, boomerang-shaped regions related to specified intervals of connection lengths, which are

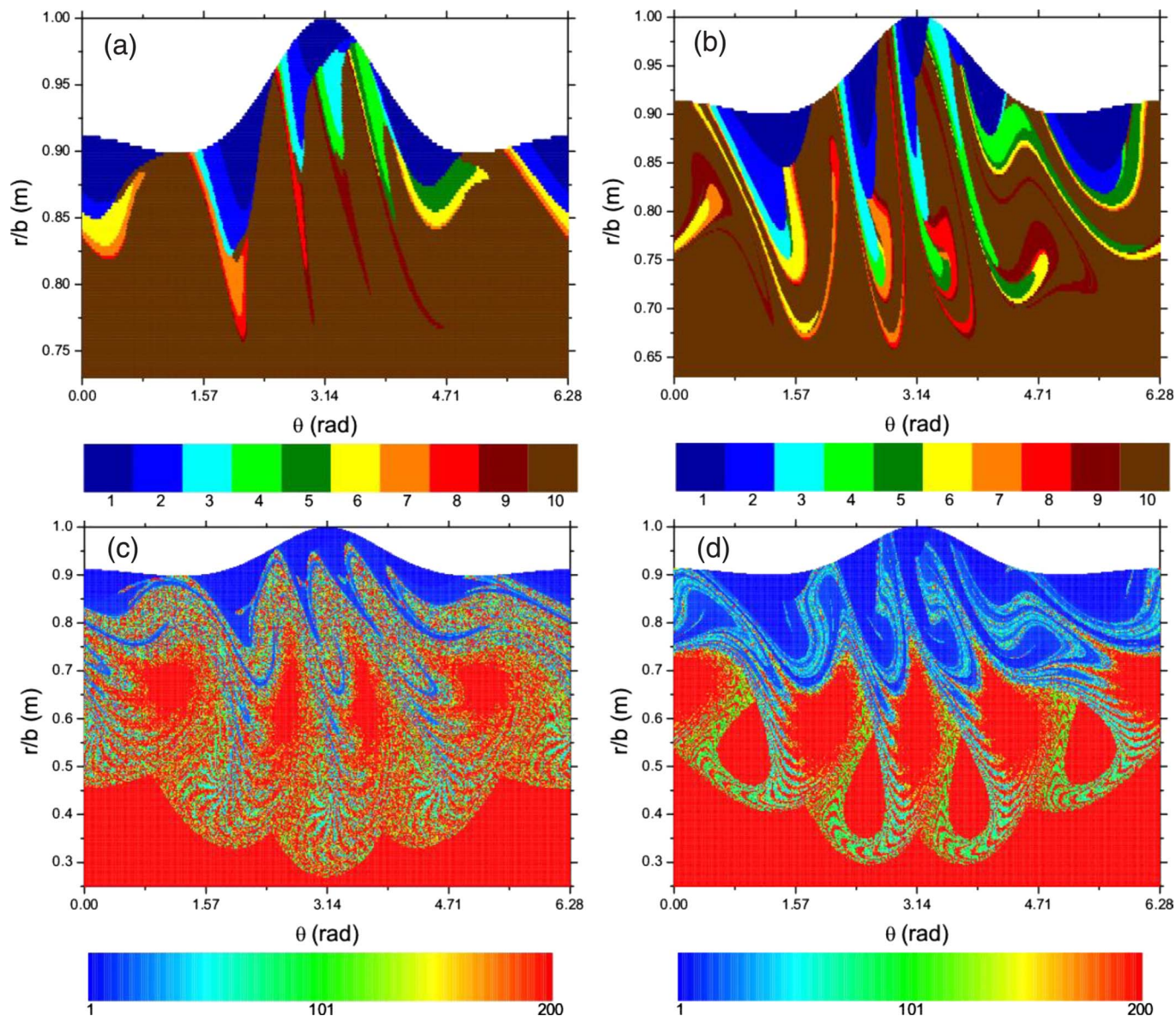


FIG. 7. (Color online) Distribution of connection lengths in the range $[1, 10]$ (indicated by a color scale) for the Poincaré sections depicted in (a) Fig. 4(a); (b) Fig. 4(b). (c) and (d) represent this distribution in the range $[1, 200]$ for (a) and (b), respectively.

similar to those experimentally identified in tokamaks.^{38,70} Figures 8(a) and 8(b) indicate a high concentration of regions with large connection lengths for the (4,1) perturbation mode. On the other hand, Figs. 8(c) and 8(d), obtained for the (5,1) mode, suggest a scattering of these regions over a larger poloidal extension. In order to understand the color changes seen in Fig. 8(b), we present from Figs. 9(a)–9(d) the Poincaré sections corresponding to the values of the edge safety factor $q(a)=4.5, 4.3, 3.9,$ and $3.2,$ respectively. They indicate that the last remnant island chains, near the internal KAM surfaces, where the concentration of field lines is more pronounced, have mode numbers (4,1) and (11,3) [Fig. 9(a)], (7,2) [Fig. 9(b)], (10,3) [Fig. 9(c)], and (3,1) [Fig. 9(d)].

For $q(a)=5.0,$ as can be seen in Fig. 4(a), one has regions with high connection lengths. The escape of the field lines is essentially determined by the homoclinic tangle of the dimerized main chain (4,1). This conclusion is also drawn from the results shown by Fig. 8(b), where there is a

dominant ergodic region near the tokamak wall. A general trait observed in Fig. 9 is that, as the value of $q(a)$ is decreased, there follows that the size of the ergodic region diminishes and a laminar region becomes dominant. In Fig. 9(a), for $q(a)=4.5,$ the (4,1) and (11,3) chains are observed near the KAM surfaces. Thus, as can be also verified in Figs. 9(b)–9(d), the last chains next to the KAM surfaces determine the connection lengths and the escape of the field lines. In Figs. 9(b) and 9(c) this process is more evident than in Fig. 9(a). In particular, we observe from Fig. 9(d) that the (3,1) secondary dimerized chain is the dominant one.

The observed distribution of the field lines concentrated around the remnant island chains, i.e., the *stickiness*, refers to the existence of field lines in the chaotic region which spend a comparatively large time (measured in number of toroidal turns) bouncing around the vicinity of partially destroyed magnetic islands.⁷¹ Stickiness is a rather general property of the chaotic orbits of nonhyperbolic area-preserving maps,

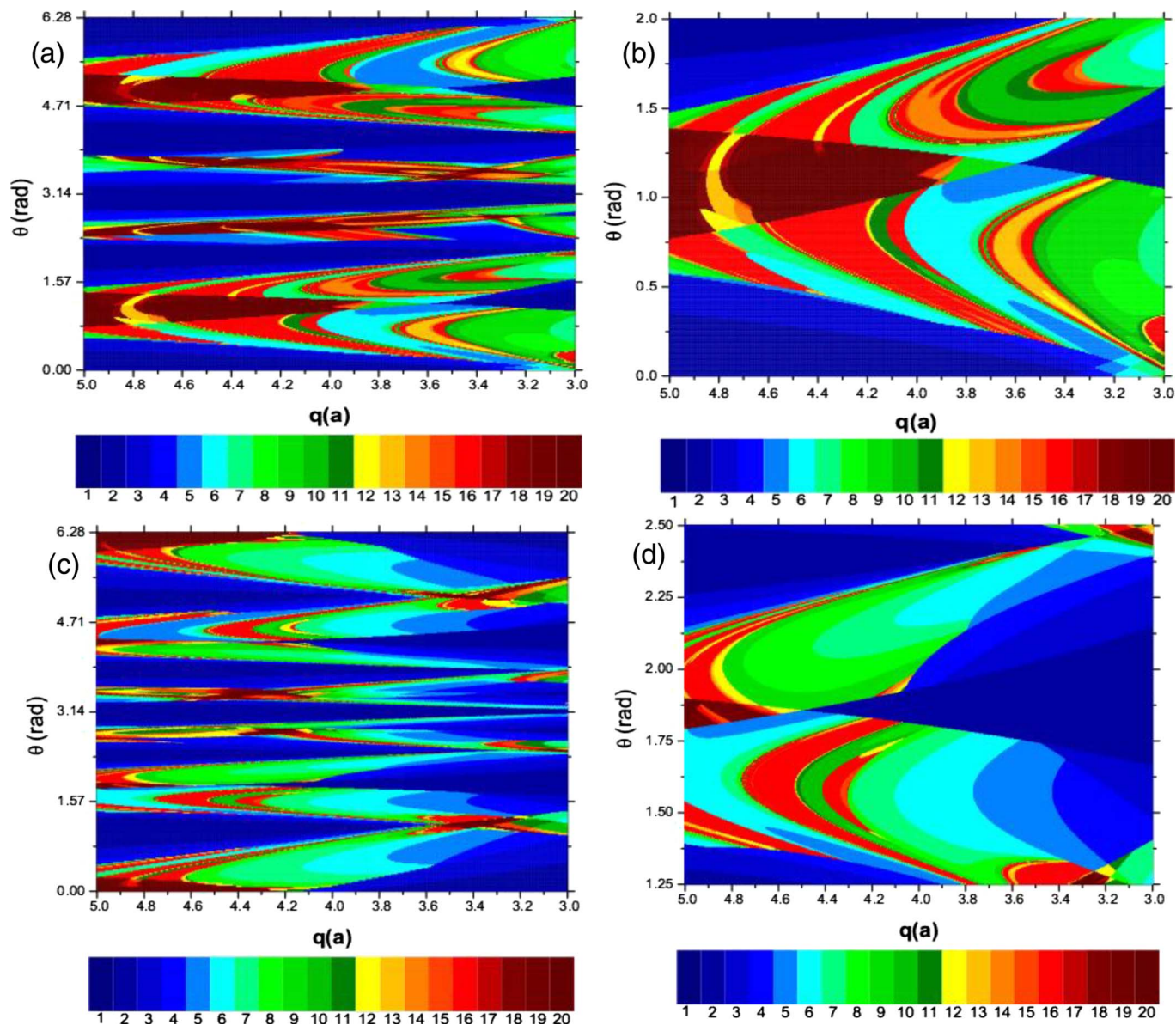


FIG. 8. (Color online) Intervals of the same connection length (indicated by a color scale) computed at the tokamak wall, as a function of the edge safety factor, and corresponding to the Poincaré sections depicted in (a) Fig. 4(a); (c) Fig. 4(b). (b) and (d) are magnifications of a region in (a) and (c), respectively.

and produces a nonuniform distribution of points in the chaotic region.⁷²

In the context of the present work, stickiness is one of the causes of the appearance of regions with large connection lengths. Another factor contributing to the highly concentrated connection length intervals in Figs. 8(a) and 8(b) is the existence of the escape channels that drive field lines from the stickiness regions towards the wall. The more scattered escape regions depicted in Figs. 9(a) and 9(b) imply larger values of the corresponding average connection length, in comparison with the more concentrated regions observed in Figs. 9(c) and 9(d). The observed distinctions are due to the differences between the stickiness regions and the escape channels located at the remnant's last island chains. As pointed in Ref. 70 these distinctions come from the different manifold tangles underlying their chaotic orbits, as already suggested from the chaotic saddles depicted in Figs. 5 and 6. Moreover, the last island chains change with the value of

$q(a)$, since these chains correspond to different mode numbers (m, n) for the perturbation magnetic field, from (4,1), (11,3) [Fig. 9(a)], to (3,1) [Fig. 9(d)]. Thus, the strong dependence of boomerang structures on the edge safety factor variation, that is observed in Fig. 8, is explained by the sequence of island chains that successively become dominant as the safety factor decreases.

Figure 10 shows the poloidal wave number power spectrum variation with $q(a)$ of selected field lines with long connection lengths. For each $q(a)$ we determine the connection lengths of many field lines starting on the wall and initial poloidal angles distributed uniformly. Next, for each $q(a)$, we select the field line with the longest connection length and calculate its Fourier spectrum. This choice was motivated by the observed line stickiness around the dominant island chain that explains the long connection length.

For each $q(a)$ in the intervals with a dominant frequency

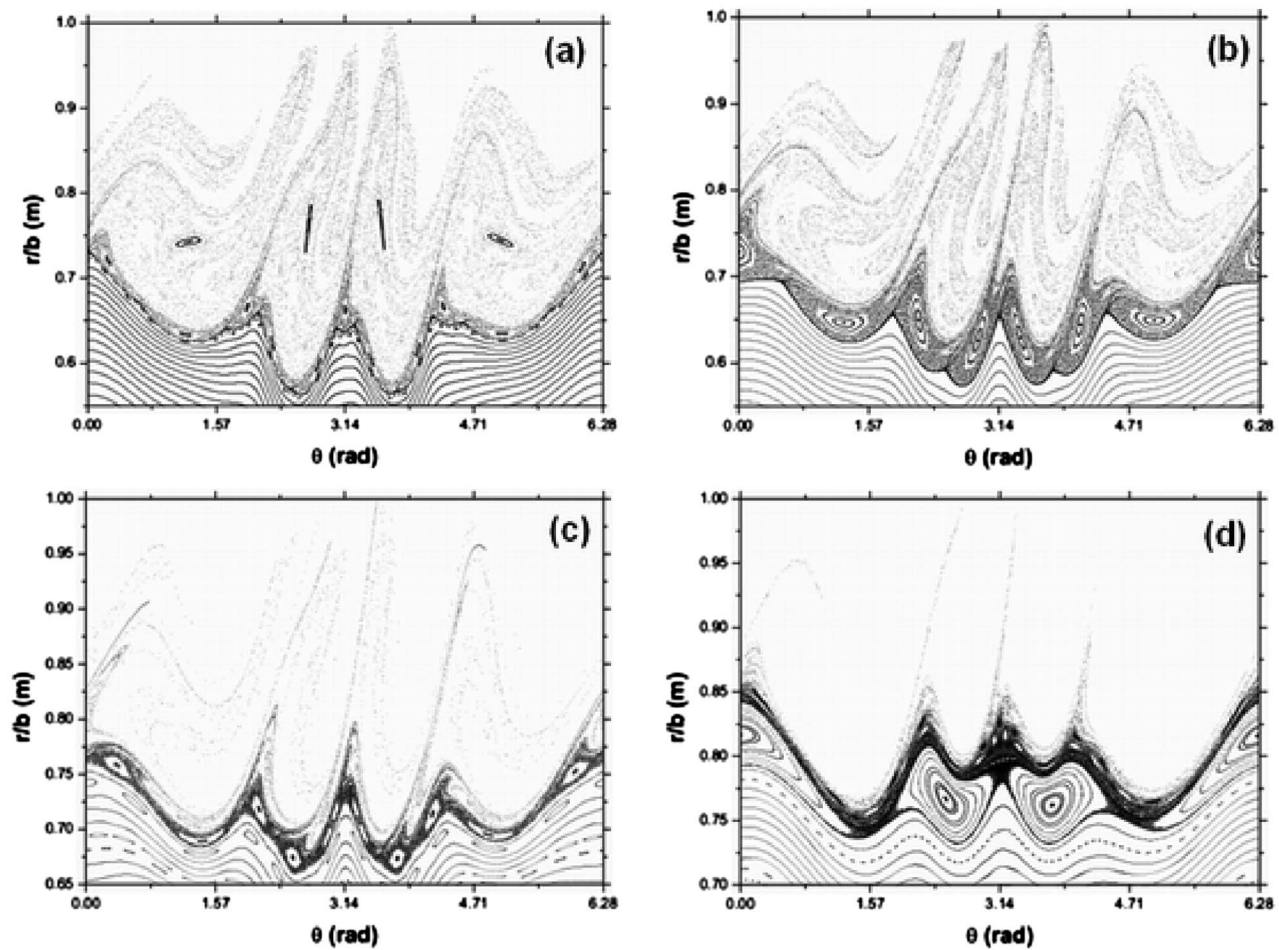


FIG. 9. Magnifications of the Poincaré sections corresponding to four points of Fig. 8(b) for (a) $q(a)=4.5$, (b) $q(a)=4.3$, (c) $q(a)=3.9$, and (d) $q(a)=3.2$.

in the power spectral analysis, we use the computed frequency to calculate (from its inverse) the trapped line rotational transform. The rotational transforms, obtained by this procedure, are rational numbers (indicated by arrows in Fig. 10, where plateaus indicate the edge safety factor for which a

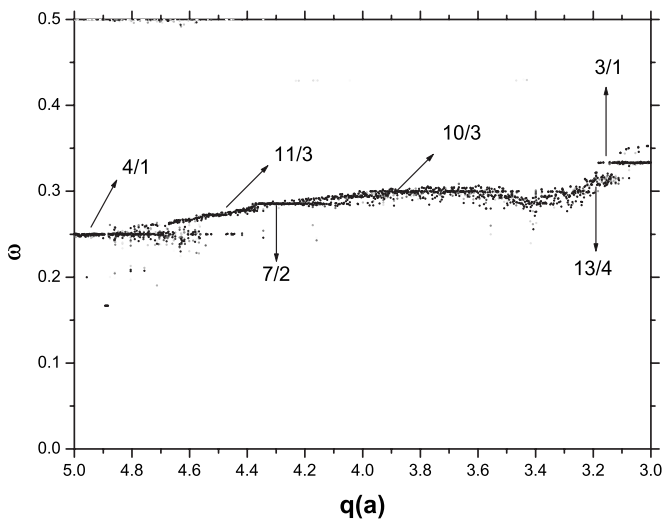


FIG. 10. Power spectral variation with $q(a)$ between 5.0 and 3.0, for selected field lines with long connection lengths.

dominant frequency exists). These rational values are equal to those obtained for the dominant island chains where the corresponding field lines, with long connection lengths, were trapped. Thus, although in Fig. 9(a) we identify remnant island chains with the rotational transform inverses (4,1) and (11,3), from the spectral analysis we obtain a rotational transform inverse of (11,3), as indicated in Fig. 10. This indicates that the dominant 11/3 island chain is the responsible for the line stickiness observed in Fig. 9(a). However, as it can also be seen in Fig. 9(a), the escape channel of the line trapped on the island chain (11,3) is determined by the (4,1) chain. Consequently, the internal remnant chain determines the connection length and the external remnant chain determines the escape channels through which the field lines leave the stickiness region and reach the wall. Similar observations are valid for other values of $q(a)$. In particular, for $q(a)$ slightly above 3.0, as in Fig. 9(d), we identify the internal remnant (3,1) chain as responsible for the line stickiness, whereas the escape channels are determined by an external remnant chain. Therefore, the analysis of Figs. 9 and 10 confirm that high connection lengths are observed once some lines are trapped on internal islands during many toroidal turns. The variation of $q(a)$ changed the topology of the dominant islands and the associated stickiness, consequently, also changing the connection lengths. Moreover, the substructures on

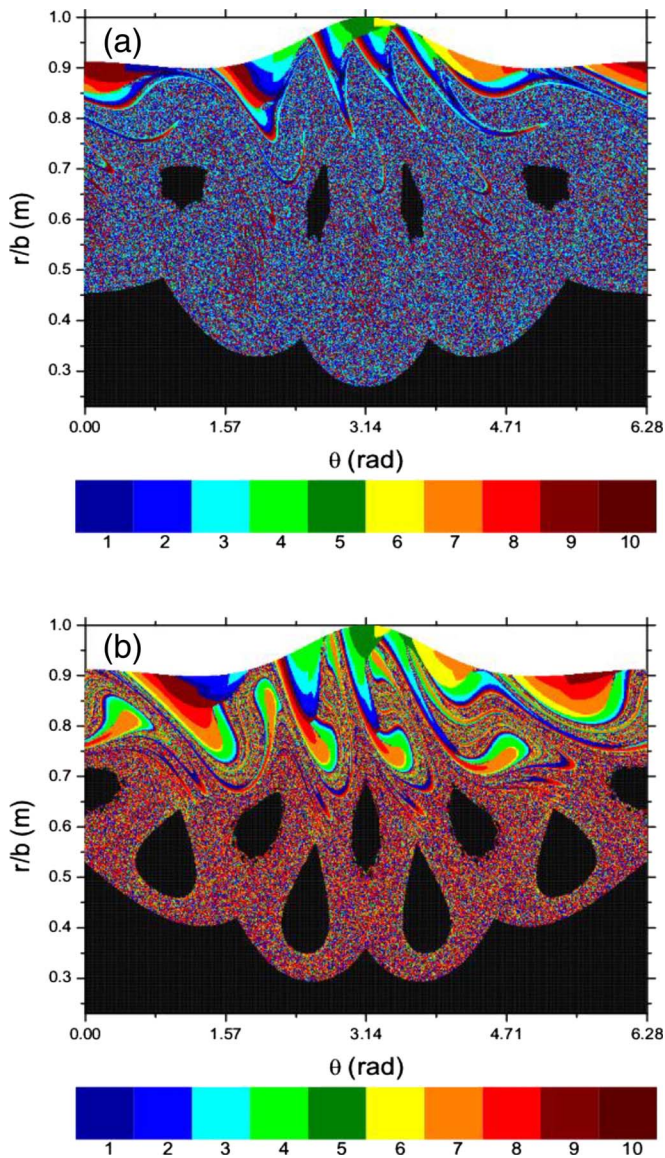


FIG. 11. (Color online) Exit basins dividing the poloidal cross section into ten regions (indicated by a color scale), corresponding to the Poincaré sections depicted in (a) Fig. 4(a); (b) Fig. 4(b).

Fig. 8 can be related to ranges of the edge safety factor $q(a)$ for which dominant islands are found.

Another way to complement this discussion is to relate the distribution of connection lengths with the exit basins and magnetic footprints. The exit basins correspond to a set of initial conditions which generates field lines that escape through a given exit. We obtained such basins by dividing the tokamak wall at a given toroidal section into ten intervals of equal poloidal extension. Any interval can be viewed as an exit, and all the initial conditions leading to field lines escaping through that exit are depicted with the same color. Figures 11(a) and 11(b) show the exit basins corresponding to these ten intervals (in a color scale), for $I_h/I_p=0.11$, and a limiter with mode numbers (4,1) and (5,1), respectively. The field lines in Fig. 11(a) which do not escape after less than 4000 iterations are marked in black.

We can see in Fig. 11(a) that the ten exit basins are intertwined in a very complex way, with a fractal pattern

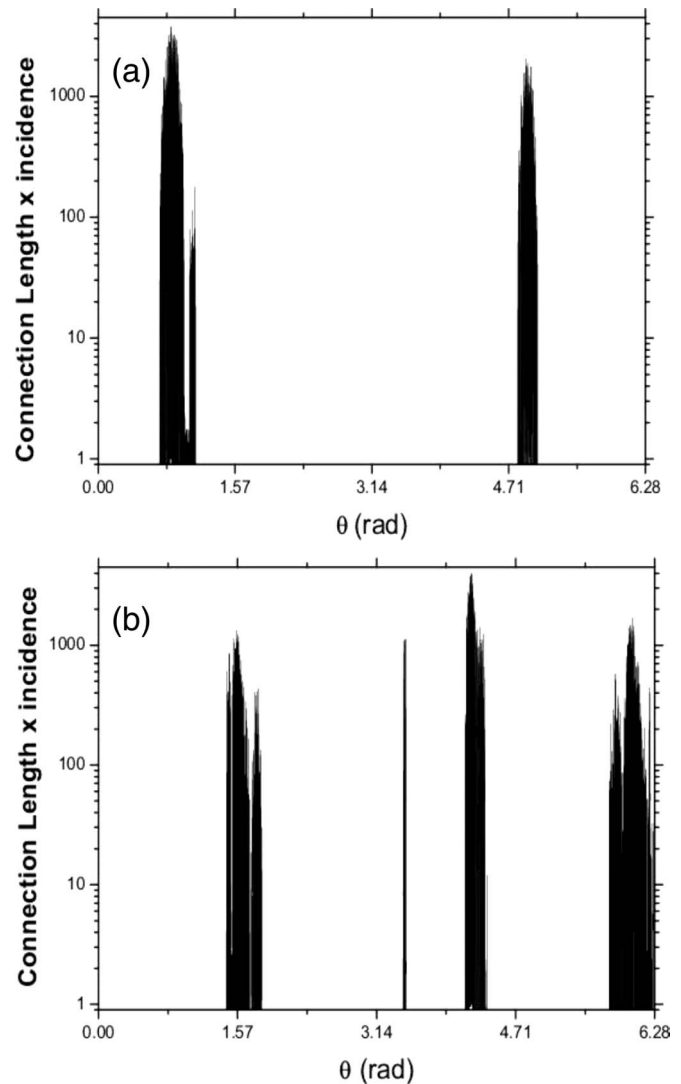


FIG. 12. Histograms for the number of escaping field lines times their connection lengths, corresponding to the Poincaré sections depicted in (a) Fig. 4(a); (b) Fig. 4(b).

very similar to that observed in the corresponding distribution of the connection lengths [see Fig. 7(c)]. When the perturbing mode number is (5,1) [Fig. 11(b)], the escape channels are much more scattered than in the (4,1) mode, as can be observed also for the distribution of the connection lengths. We notice that lines coming from the inner part of the plasma column reach a concentrated region of the tokamak wall, as illustrated in Figs. 11(a) and 11(b), and contributing significantly to the localized heat deposition on the wall.

The magnetic footprints also help us to understand the escape channels for different mode numbers of the perturbation field. They are the deposition patterns of the field lines from the chaotic region and which are lost due to collisions with the wall. A statistical characterization of the magnetic footprints is shown in Figs. 12(a) and 12(b), depicting histograms for the number of the lost field lines multiplied by their connection lengths for perturbation currents of $I_h/I_p=0.11$ and the mode numbers (4,1) and (5,1), respectively. In the former case, there are four dimerized island chains, each

of them with a characteristic stickiness region and (due to the safety factor profile) with a nonuniform poloidal distribution. In fact, even though we expect out of four escape channels, we have basically two regions of large statistical incidence [two broad peaks in Fig. 12(a)]. A similar conclusion is drawn from the peaks observed in Fig. 12(b), for which five escape channels are expected. Our approximate Hamiltonian with delta kicks is not able to reproduce a helical structure of magnetic footprints on the wall along the toroidal and poloidal axes, found, for instance, in Ref. 41.

V. CONCLUSIONS

In tokamaks with reversed magnetic shear at the plasma edge, high amplitude perturbations are necessary to destroy the external invariant magnetic surface that confine the plasma. Thus, this convenient stability property encourages the use of nonmonotonic plasma current density to generate enhanced confinement regimes with levels of particle and heat transport much lower than those commonly observed in experiments.

However, even for reversed shear equilibria, as those considered in this paper, external surfaces are destroyed by resonant perturbations through a breakup scenario common to nontwist Hamiltonian systems, and which yields localized (Lagrangian) chaos. Furthermore, for these equilibria, we analyzed how the magnetic field lines escape to the wall through the so-called laminar and ergodic regions (those with short and long connection lengths, respectively) located between the most external surviving island chain and the tokamak wall. Thus, the field line with long connection lengths may escape to the wall transporting energetic particles from the plasma interior. Moreover, the line stickiness and the escape channels to the wall are a consequence of a series of internal dominant island chains, near the KAM barriers inside the plasma. For several equilibrium configurations, it was possible to identify that the line stickiness depends on a remnant internal island chain, while the escape channels are determined by a remnant external island chain.

We showed that the field line connection lengths to the wall depend on the homoclinic tangle around the last remnant island chain. This dependence may create an undesirable difficulty, since the use of nonmonotonic current density profiles combined with resonant perturbations may create extremely concentrated magnetic footprints on the tokamak wall, thus possibly worsening problems related with heat and particle loading in the wall.

In conclusion, we presented a procedure to evaluate the possible undesirable concentration of the expected magnetic footprints on the wall, given the equilibrium and perturbation parameters. To show the dependence of this effect on the edge safety factor, the internal island chains were identified by their rotational transform and associated to the strike zones on the tokamak wall. Our numerical simulations were made for nonmonotonic analytical toroidal equilibria, perturbed by resonances created by an ergodic limiter. However, the presented analysis and the conclusions are valid for other kinds of resonant perturbations, as those created by a divertor or due to natural MHD oscillations.

ACKNOWLEDGMENTS

This work was made possible through partial financial support from the following Brazilian research agencies: FAPESP (São Paulo), CAPES, CNPq, and Fundação Araucária (Paraná).

- ¹F. M. Levinton, M. C. Zarnstorff, S. H. Batha, M. Bell, R. E. Bell, R. V. Budny, C. Bush, Z. Chang, E. Fredrickson, A. Janos, J. Manickam, A. Ramsey, S. A. Sabbagh, G. L. Schmidt, E. J. Synakowski, and G. Taylor, *Phys. Rev. Lett.* **75**, 4417 (1995).
- ²E. J. Strait, L. L. Lao, M. E. Mauel, B. W. Rice, T. S. Taylor, K. H. Burrell, M. S. Chu, E. A. Lazarus, T. H. Osborne, S. J. Thompson, and A. D. Turnbull, *Phys. Rev. Lett.* **75**, 4421 (1995).
- ³E. Mazzucato, S. H. Batha, M. Beer, M. Bell, R. E. Bell, R. V. Budny, C. Bush, T. S. Hahm, G. W. Hammett, F. M. Levinton, R. Nazikian, H. Park, G. Rewoldt, G. L. Schmidt, E. J. Synakowski, W. M. Tang, G. Taylor, and M. C. Zarnstorff, *Phys. Rev. Lett.* **77**, 3145 (1996).
- ⁴P. H. Diamond, V. B. Lebedev, D. E. Newman, B. A. Carreras, T. S. Hahm, W. M. Tang, G. Rewoldt, and K. Avinash, *Phys. Rev. Lett.* **78**, 1472 (1997).
- ⁵P. Mantica, G. Gorini, F. Imbeaux, J. Kinsey, Y. Sarazin, R. Budny, I. Coffey, R. Dux, X. Garbet, L. Garzotti, C. Ingesson, M. Kissick, V. Parail, C. Sozzi, A. Walden, and contributors to the EFDA-JET Workprogramme, *Plasma Phys. Controlled Fusion* **44**, 2185 (2002).
- ⁶W. Kerner and H. Tasso, *Phys. Rev. Lett.* **49**, 654 (1982).
- ⁷A. C. C. Sips, for the Steady State Operation, and the Transport Physics topical groups of the International Tokamak Physics Activity, *Plasma Phys. Controlled Fusion* **47**, A19 (2005).
- ⁸F. A. Marcus, T. Kroetz, M. Roberto, I. L. Caldas, E. C. da Silva, R. L. Viana, and Z. O. Guimarães-Filho, *Nucl. Fusion* **48**, 24018 (2008).
- ⁹Special Issue of reversed shear configuration in large tokamaks published in *Plasma Phys. Controlled Fusion*, Vol. 47 (2002).
- ¹⁰F. Karger and K. Lackner, *Phys. Lett.* **61A**, 385 (1977).
- ¹¹Ph. Ghendrih, M. Bécoulet, L. Colas, A. Grosman, R. Guirlet, J. Gunn, T. Loarer, A. Azéroual, V. Basiuk, B. Beaumont, A. Bécoulet, P. Beyer, S. Brémond, J. Bucalossi, H. Capes, Y. Corre, L. Costanzo, C. De Michelis, P. Devynck, S. Féron, C. Friant, X. Garbet, R. Giannela, C. Grisolia, W. Hess, J. Hogan, L. Ladurelle, F. Laugier, G. Martin, M. Mattioli, B. Meslin, P. Monier-Garbet, D. Moulin, F. Nguyen, J.-Y. Pascal, A.-L. Pecquet, B. Pégourié, R. Reichle, F. Saint-Laurent, J.-C. Vallet, M. Zabiégo, and Tore Supra Team, *Nucl. Fusion* **42**, 1221 (2002).
- ¹²A. Grosman, J.-M. Ané, P. Barabaschi, K. H. Finken, A. Mahdavi, Ph. Ghendrih, G. Huysmans, M. Lipa, P. R. Thomas, and E. Tsitroni, *J. Nucl. Mater.* **313–316**, 314 (2003).
- ¹³C. J. A. Pires, E. A. O. Saettone, M. Y. Kucinski, A. Vannucci, and R. L. Viana, *Plasma Phys. Controlled Fusion* **47**, 1609 (2005).
- ¹⁴T. E. Evans, M. Goniche, A. Grosman, D. Guilhem, W. Hess, and J.-C. Vallet, *J. Nucl. Mater.* **196–198**, 421 (1992).
- ¹⁵T. C. Hender, R. Fitzpatrick, A. W. Morris, P. G. Carolan, R. D. Durst, T. Edlington, J. Ferreira, S. J. Fielding, P. S. Haynes, J. Hugill, I. J. Jenkins, R. J. La Haye, B. J. Parham, D. C. Robinson, T. N. Todd, M. Valovic, and G. Vayakis, *Nucl. Fusion* **32**, 2091 (1992).
- ¹⁶F. Karger, H. Wobig, and S. Corti, in *Proceeding of the 6th International Conference on Plasma Physics and Controlled Nuclear Fusion Research*, 1973 (IAEA, Tokyo, 1974), Vol. 1, p. 207; Pulsator Team, *Nucl. Fusion* **25**, 1059 (1985).
- ¹⁷D. C. Robinson, *Nucl. Fusion* **25**, 1101 (1985).
- ¹⁸A. Vannucci, I. C. Nascimento, and I. L. Caldas, *Plasma Phys. Controlled Fusion* **31**, 147 (1989).
- ¹⁹S. C. McCool, A. J. Wootton, A. Y. Aydemir, R. D. Bengtson, J. A. Boedo, R. V. Bravenec, D. L. Brower, J. S. Degraessie, T. E. Evans, S. P. Fan, J. C. Forster, M. S. Foster, K. W. Gentle, Y. X. He, R. L. Hickock, R. G. L. Jackson, S. K. Kim, M. Kotschenreuther, N. C. Luhmann, W. H. Miner, N. Ohyabu, D. M. Patterson, W. A. Peebles, P. E. Phillips, T. L. Rhodes, B. Richards, C. P. Ritz, D. W. Ross, W. L. Rowan, P. M. Schoch, B. A. Smith, J. C. Wiley, X. H. Yu, and S. B. Zheng, *Nucl. Fusion* **29**, 547 (1989).
- ²⁰T. E. Evans, R. A. Moyer, P. R. Thomas, J. G. Watkins, T. H. Osborne, J. A. Boedo, E. J. Doyle, M. E. Fenstermacher, K. H. Finken, R. J. Groebner, M. Groth, J. H. Harris, R. J. La Haye, C. J. Lasnier, S. Masuzaki, N. Ohyabu, D. G. Pretty, T. L. Rhodes, H. Reimerdes, D. L. Rudakov, M. J. Schaffer, G. Wang, and L. Zeng, *Phys. Rev. Lett.* **92**, 235003 (2004).

- ²¹P. Ghendrih, A. Grossman, and H. Capes, *Plasma Phys. Controlled Fusion* **38**, 1653 (1996).
- ²²A. Grosman, *Plasma Phys. Controlled Fusion* **41**, A185 (1999).
- ²³P. Ghendrih, M. Bécoulet, L. Costanzo, Y. Corre, C. Grisolia, A. Grosman, R. Guirlet, J. P. Gunn, T. Loarer, P. Monier-Garbet, P. R. Thomas, M. Zabiégo, J. Bucalossi, P. Devynck, G. Martin, C. De Michelis, F. Nguyen, B. Pégourié, R. Reichle, F. Saint-Laurent, J.-C. Vallet, and Tore Supra Team, *Nucl. Fusion* **41**, 1401 (2001).
- ²⁴A. V. Nedospasov and M. Z. Tokar, *J. Nucl. Mater.* **93–94**, 248 (1980).
- ²⁵S. Takamura, Y. Kikuchi, Y. Uesugi, and M. Kobayashi, *Nucl. Fusion* **43**, 393 (2003).
- ²⁶T. Shoji, H. Tamai, Y. Miura, M. Mori, H. Ogawa, A. W. Leonard, T. Jensen, A. W. Hyatt, A. M. Howald, G. Fuchs, N. Ohya, N. Asakura, T. Fujita, M. Shimada, S. Tsuji, H. Maeda, H. Aikawa, K. Hoshino, S. Kasai, T. Kawakami, H. Kawashima, M. Maeno, T. Matsuda, T. Ogawa, T. Seike, N. Suzuki, K. Uehara, T. Yamamoto, T. Yamauchi, T. Hamano, K. Hasegawa, A. Honda, M. Kazawa, Y. Kashiwa, K. Kikuchi, H. Okano, E. Sato, N. Seki, T. Shibata, T. Shiina, S. Suzuki, T. Tani, T. Tokutake, Y. Tomiyama, and T. Yamasato, *J. Nucl. Mater.* **196–198**, 296 (1992).
- ²⁷S. Takamura, Y. Shen, H. Yamada, M. Miyake, T. Tamakoshi, and T. Okuda, *J. Nucl. Mater.* **162–164**, 643 (1989).
- ²⁸A. Grosman, Ph. Ghendrih, B. Meslin, and D. Guilhem, *J. Nucl. Mater.* **241–243**, 532 (1997).
- ²⁹T. E. Evans, R. K. W. Roeder, J. A. Carter, and B. I. Rapoport, *Contrib. Plasma Phys.* **44**, 235 (2004).
- ³⁰T. E. Evans, R. K. W. Roeder, J. A. Carter, B. I. Rapoport, M. E. Fenstermacher, and C. J. Lasnier, *J. Phys.: Conf. Ser.* **7**, 174 (2005).
- ³¹I. Joseph, T. E. Evans, A. M. Runov, M. E. Fenstermacher, M. Groth, S. V. Kasilov, C. J. Lasnier, R. A. Moyer, G. D. Porter, M. J. Schaffer, R. Schneider, and J. G. Watkins, *Nucl. Fusion* **48**, 045009 (2008).
- ³²K. H. Finken, S. S. Abdullaev, M. F. M. De Bock, B. Giesen, M. Von Hellermann, G. M. D. Hogeweij, M. Jakubowski, R. Jaspers, M. Kobayashi, H. R. Koslowski, M. Lehnen, G. Matsunaga, O. Neubauer, A. Pospieszczyk, U. Samm, B. Schweer, and R. Wolf, *Fusion Sci. Technol.* **47**, 87 (2005).
- ³³R. C. Wolf, W. Biel, M. F. M. de Bock, K. H. Finken, S. Günter, G. M. D. Hogeweij, S. Jachmich, M. W. Jakubowski, R. J. E. Jaspers, A. Krämer-Flecken, H. R. Koslowski, M. Lehnen, Y. Liang, B. Unterberg, S. K. Varshney, M. von Hellermann, Q. Yu, O. Zimmermann, S. S. Abdullaev, A. J. H. Donné, U. Samm, B. Schweer, M. Tokar, E. Westerhof, and the TEXTOR Team, *Nucl. Fusion* **45**, 1700 (2005).
- ³⁴K. H. Finken, S. S. Abdullaev, M. Jakubowski, M. Lehnen, A. Nicolai, and K. H. Spatschek, *The Structure of Magnetic Fields in the TEXTOR-DED* (Forschungszentrum, Jülich, 2005), Vol. 45, available online at <http://www.fz-juelich.de/zb/datapool/page/439/00312Finken.pdf>.
- ³⁵K. H. Finken, B. Unterberg, Y. Xu, S. S. Abdullaev, M. Jakubowski, M. Lehnen, M. F. M. de Bock, S. Bozhnikov, S. Brezinsek, C. Busch, I. G. J. Classen, J. W. Coenen, D. Harting, M. von Hellermann, S. Jachmich, R. J. E. Jaspers, Y. Kikuchi, A. Krämer-Flecken, Y. Liang, M. Mitri, P. Peleman, A. Pospieszczyk, D. Reiser, D. Reiter, U. Samm, D. Schega, O. Schmitz, S. Soldatov, M. Van Schoor, M. Vergote, R. R. Weynants, R. Wolf, O. Zimmermann, and the TEXTOR Team, *Nucl. Fusion* **47**, 522 (2007).
- ³⁶K. H. Finken, S. S. Abdullaev, M. W. Jakubowski, M. F. M. de Bock, S. Bozhnikov, C. Busch, M. von Hellermann, R. Jaspers, Y. Kikuchi, A. Krämer-Flecken, M. Lehnen, D. Schega, O. Schmitz, K. H. Spatschek, B. Unterberg, A. Wingen, R. C. Wolf, and O. Zimmermann, *Phys. Rev. Lett.* **98**, 065001 (2007).
- ³⁷S. S. Abdullaev, K. H. Finken, M. W. Jakubowski, S. V. Kasilov, M. Kobayashi, D. Reiser, D. Reiter, A. M. Runov, and R. Wolf, *Nucl. Fusion* **43**, 299 (2003).
- ³⁸A. Wingen, K. H. Spatschek, and S. S. Abdullaev, *Contrib. Plasma Phys.* **45**, 500 (2005).
- ³⁹E. C. da Silva, M. Roberto, I. L. Caldas, and R. L. Viana, *Phys. Plasmas* **13**, 052511 (2006).
- ⁴⁰S. S. Abdullaev, *Construction of Mappings for Hamiltonian Systems and Their Applications* (Springer, Berlin, 2006).
- ⁴¹S. S. Abdullaev, T. Eich, and K. H. Finken, *Phys. Plasmas* **8**, 2739 (2001).
- ⁴²K. H. Finken, T. Eich, and A. Kaleck, *Nucl. Fusion* **38**, 515 (1998).
- ⁴³S. S. Abdullaev and K. H. Finken, *Nucl. Fusion* **38**, 531 (1998).
- ⁴⁴S. S. Abdullaev and G. M. Zaslavsky, *Phys. Plasmas* **3**, 516 (1996).
- ⁴⁵B. J. Brams and M. D. Teytel, "Investigation of the effect of external magnetic perturbation upon divertor heat load," in Proceedings of the International Sherwood Fusion Theory Conference, Newport, Rhode Island, 1993, p. 1C21.
- ⁴⁶N. Pomphrey and A. Reiman, *Phys. Fluids B* **4**, 938 (1992).
- ⁴⁷H. Ali, A. Punjab, A. Boozer, and T. Evans, *Phys. Plasmas* **11**, 1908 (2004).
- ⁴⁸A. Punjab, H. Ali, and A. Boozer, *Phys. Plasmas* **4**, 337 (1997).
- ⁴⁹J. S. E. Portela, I. L. Caldas, and R. L. Viana, "Tokamak magnetic field line structure described by simple maps," *Eur. Phys. J. Spec. Top.* (unpublished).
- ⁵⁰M. Roberto, E. C. da Silva, I. L. Caldas, and R. L. Viana, *Physica A* **342**, 363 (2004).
- ⁵¹E. C. da Silva, I. L. Caldas, R. L. Viana, and M. A. F. Sanjuan, *Phys. Plasmas* **9**, 4917 (2002).
- ⁵²D. del-Castillo-Negrete, J. M. Greene, and P. J. Morrison, *Physica D* **91**, 1 (1996); **100**, 311 (1997).
- ⁵³G. A. Oda and I. L. Caldas, *Chaos, Solitons Fractals* **5**, 15 (1995); G. Corso, G. A. Oda, and I. L. Caldas, *ibid.* **8**, 1891 (1997).
- ⁵⁴P. J. Morrison, *Rev. Mod. Phys.* **70**, 467 (1998); *Phys. Plasmas* **7**, 2279 (2000).
- ⁵⁵J. Meiss, *Rev. Mod. Phys.* **64**, 795 (1992).
- ⁵⁶J. E. Howard and S. M. Hohns, *Phys. Rev. A* **29**, 418 (1984).
- ⁵⁷A. J. Lichtenberg and M. A. Leiberman, *Regular and Chaotic Dynamics*, 2nd ed. (Springer Verlag, New York, 1992).
- ⁵⁸R. Balescu, *Phys. Rev. E* **58**, 3781 (1998).
- ⁵⁹L. E. Reichl, *The Transition to Chaos* (Springer Verlag, Berlin, 2004).
- ⁶⁰M. Y. Kucinski, I. L. Caldas, L. H. A. Monteiro, and V. Okano, *J. Plasma Phys.* **44**, 303 (1990).
- ⁶¹E. C. da Silva, I. L. Caldas, and R. L. Viana, *Phys. Plasmas* **8**, 2855 (2001).
- ⁶²M. Roberto, E. C. da Silva, I. L. Caldas, and R. L. Viana, *Phys. Plasmas* **11**, 214 (2004).
- ⁶³T. J. Stucchi, *Braz. J. Phys.* **32**, 958 (2002).
- ⁶⁴E. C. da Silva, I. L. Caldas, and R. L. Viana, *IEEE Trans. Plasma Sci.* **29**, 617 (2001).
- ⁶⁵M. Roberto, E. C. da Silva, I. L. Caldas, and R. L. Viana, *J. Phys.: Conf. Ser.* **7**, 163 (2005).
- ⁶⁶E. C. da Silva, M. Roberto, I. L. Caldas, and R. L. Viana, *Phys. Plasmas* **13**, 052511 (2006).
- ⁶⁷S. Bleher, C. Grebogi, E. Ott, and R. Brown, *Phys. Rev. A* **38**, 930 (1988).
- ⁶⁸S. S. Abdullaev, K. H. Finken, A. Kaleck, and K. H. Spatschek, *Phys. Plasmas* **5**, 196 (1998).
- ⁶⁹M. W. Jakubowski, S. S. Abdullaev, K. H. Finken, M. Lehnen, and the TEXTOR Team, *J. Nucl. Mater.* **337–339**, 532 (2005).
- ⁷⁰A. Wingen, M. Jakubowski, K. H. Spatschek, S. S. Abdullaev, K. H. Finken, and A. Lehnen, *Phys. Plasmas* **14**, 042502 (2007).
- ⁷¹G. M. Zaslavsky, *Phys. Rep.* **371**, 461 (2002).
- ⁷²J. D. Szezech, Jr., S. R. Lopes, and R. L. Viana, *Phys. Lett. A* **335**, 394 (2005).